Nuclear Engineering and Technology 56 (2024) 4115–4126

Contents lists available at ScienceDirect

Nuclear Engineering and Technology

journal homepage: www.elsevier.com/locate/net

Original Article

Swelling at high radiation damage levels of 120 and 240 dpa in 3.5 MeV self-ion irradiated ferritic/martensitic steels

Myeongkyu Lee [a,b], Geon Kim [a,c], Sangjoon Ahn [a,*]

[a] Department of Nuclear Engineering, Ulsan National Institute of Science and Technology, Ulju, Ulsan, 44919, Republic of Korea
[b] United Kingdom Atomic Energy Authority, Culham Campus, Abingdon, Oxfordshire, OX14 3DB, United Kingdom
[c] Nuclear Fuel Design Department, KEPCO Nuclear Fuel, Yuseong, Daejeon, 34057, Republic of Korea

ARTICLE INFO

Keywords:
Ferritic/martensitic steels
Fast reactor cladding material
Ion irradiation
Swelling
Bimodal cavity size distribution

ABSTRACT

The swelling behavior of ferritic/martensitic steels (FC92–B/-N, HT9, and Gr.92) was investigated following 3.5 MeV Fe^{++} ion irradiation. Tested alloys were helium-pre-implanted up to the peak contents of 120 and 240 appm with He/dpa ratio of 1 appm/dpa at room temperature and then exposed to self-ion beam to the peak damage conditions of 120 and 240 dpa at 475 °C. Field-emission transmission electron microscopy was used to characterize the cavity evolution. FC92–B exhibited the highest resistance to swelling among the irradiated alloys. The final volumetric swelling of FC92–B reached 1.3 % at 70 dpa and 2.9 % at 140 dpa. On the other hand, HT9 exhibited the highest swelling, reaching 7.4 % at 140 dpa. Comparing the present swelling results at 140 dpa/140 appm He with swelling data at 280 dpa/280 appm He from our previous study, it was observed that Gr.92 and FC92–N swelled more at 140 dpa/140 appm He than at 280 dpa/280 appm He. This negative correlation between swelling and dose in Gr.92 and FC92–N is primarily attributed to the helium-associated swelling suppression at higher helium concentration of 280 appm. A bimodal cavity size distribution appeared only in Gr.92 and FC92–N at 280 dpa/280 appm. This result demonstrates that the excess amount of helium over 200 appm promoted early-stabilization of new-born cavities, resulting in preferentially enhanced cavity nucleation, while impeding the growth of nucleated cavities. An inhibition in cavity growth possibly led to an extended duration of nucleation-dominant stages, finally suppressing swelling in ion-irradiated Gr.92 and FC92–N alloys.

1. Introduction

In-core components in the advanced-type reactor concepts, such as the sodium-cooled fast reactor (SFR), will be exposed to the harsh service conditions of high temperature to 700 °C and intense radiation damage levels over 200 dpa [1]. It is thus essential to understand the radiation response of the component materials at a high-dose regime. However, there exist some challenges to examine under-radiation behaviors of the core materials using the test reactors due to their low damage rate and high residual radioactivity after in-reactor neutron irradiation [2]. In this regard, the accelerator-based irradiating method has been spotlighted as the surrogate for neutron irradiation in that it can provide high radiation damage rate, and in turn, time-/-cost-efficiency. No (or little) residual activities as well as controllability of irradiating parameters make this accelerator-based irradiating methodology more favorable [3,4].

Ferritic/martensitic steel (F/M steel) has been considered as a leading candidate for cladding materials in the SFR systems [5]. Historically, this type of high Cr steel alloys have exhibited not only the excellent high-temperature thermophysical characteristics [6], but also the promising radiation resistance after its initial testing at the Fast Flux Test Facility (FFTF) [5]. In addition, the compatibility of F/M steels with sodium makes them desirable for the usage as a cladding material in the sodium-cooled fast reactor (SFR) systems [7]. Alloys FC92–B/-N are 9Cr-0.5Mo–2W F/M steels developed by the Korea Atomic Energy Research Institute (KAERI) for the SFR application. They exhibited >30 % improved creep properties at 650 °C as compared to that of HT9 and finally chosen as the final candidate for a fuel cladding material in the Prototype Gen-IV Sodium-cooled Fast Reactor (PGSFR) [8]. They underwent the in-reactor irradiation utilizing the BOR-60 in Russia from 2014 to 2019 and then radiation damage achieved after 6-year irradiation in BOR-60 was estimated to reach only ~75 dpa due to the intrinsic characteristics of low damage rate.

Therefore, this study aims to investigate the swelling behaviors of

* Corresponding author.
E-mail address: sjahn99@unist.ac.kr (S. Ahn).

https://doi.org/10.1016/j.net.2024.05.014
Received 5 February 2024; Received in revised form 17 April 2024; Accepted 14 May 2024
Available online 15 May 2024

newly-developed F/M steels at higher radiation damage conditions than 75 dpa, with a focus on cavity evolution, utilizing heavy ion accelerator and field-emission transmission electron microscopy (FE-TEM). Irradiation was conducted by combining 3.5 MeV self-ion beam irradiation at 475 °C up to the peak radiation damage levels of 120 and 240 dpa with helium ion pre-implantation of 1 appm/dpa at the room temperature. Two commercial alloys of HT9 (84425) and Grade 92 (Gr.92) were tested as the reference under the same irradiating conditions to comparatively assess the swelling resistance of FC92 series.

2. Materials and methods

2.1. Sample preparation

Table 1 provides the nominal compositions of the four tested alloys in weight percent. As-received F/M steel plates were provided by the KAERI and electrical-discharge machined into smaller cubes measuring 1 mmW × 1 mmL × 1 mmT. These cubes were subjected to heat treatment at 1000 °C/30 min/air-cooling, and subsequently tempered at 750 °C/60 min/air-cooling to room temperature. Prior to irradiation, the surface of the heat-treated alloy specimens was flattened up to #4000 SiC papers, followed by a stepwise polishing procedure involving 6, 3, 1, and 0.25 μm diamond suspensions and 0.02 μm colloidal silica suspension.

2.2. Ion-beam irradiation and post-irradiation characterization

Two self-ion irradiation experiments were conducted to two peak damage conditions of 120 and 240 dpa at 475 °C. The 1st experiment involved Fe^{++} ion irradiation on the two FC92 steels to achieve 120 dpa, with the pre-implanted helium contents reaching up to 120 appm He. The 2nd experiment extended the irradiation to four steels, including the two FC92 steels as well as reference steels (HT9 and Gr.92), aiming for 240 dpa with pre-implanted helium contents up to 240 appm He. Prior to self-ion irradiation, raster-scanning type helium ions were loaded onto the specimens at room temperature, using a 400-kV ion accelerator in the accelerator laboratory of Texas A&M University. The pre-implanted helium contents were varied from 0 appm at the surface to 120 and 240 appm at 1000 nm depth, respectively, achieved by altering the beam energy to maintain a He/dpa ratio of 1 appm/dpa. The helium implantation ratio of 1 appm/dpa was intended to emulate the concurrent neutron-induced (n, α) reactions occurring in fast reactor systems [9]. Subsequently, 3.5-MeV defocused Fe^{++} ion irradiation was sequentially applied to the same surface using a 1.7-MV Ionex Tandetron Accelerator. Throughout the Fe^{++} ion irradiation, sample temperature was continuously monitored at both the sample surface and the sample-mounted heating stage, maintaining it at 475 °C with an uncertainty of less than ±15 °C. The target radiation damages were 120 and 240 dpa at 1000 nm depth, respectively, while the damage rate was maintained as 1.7×10^{-3} dpa/s for both target conditions. All tested alloys were irradiated simultaneously during each irradiation session to avoid the fluctuation in irradiating parameters such as dose rate and temperature. The ion fluence required to achieve the nominal radiation damage was calculated by utilizing the Stopping and Range of ions In Matter (SRIM)-2013 code, employing the "ion distribution and quick calculation of damage" option [10], with a displacement threshold energy of 40 eV, as recommended by ASTM standard [11,12]. Fig. 1 shows the SRIM-predicted radiation damage and implanted Fe ions profiles in 3.5 MeV Fe^{++} ion-irradiated FC92–B, obtained after five repetitions while altering the random number seed to compensate for statistical fluctuations.

In order to mitigate spatial inhomogeneity in cavity evolution, more than three TEM specimens were lifted-out from the ion-irradiated surface subjected to ion irradiation. The specimens were prepared using a focused ion beam (FIB, FEI Helios 450 HP), ensuring the thickness of ~100 ± 10 nm, determined through a log-ratio model employing electron energy loss spectroscopy (EELS) [13]. TEM imaging was conducted under scanning-TEM (STEM) mode using FE-TEM (FEI Titan G2 equipped with ChemiSTEM Cs Probe.) Bright-field (BF) and high-angle annular dark-field (HAADF) images were simultaneously obtained at the STEM mode with magnifications of 14 k, 57 k, and 110 k. To characterize depth-dependent cavity evolution, each HAADF image was divided into 100-nm-thick bins and processed using ImageJ (FIJI). The area of each bubble was measured assuming spherical geometry to calculate its pseudo-diameters. In this process, the distance from the surface to the center of each bubble was considered as the position of the bubble even though some of the examined bubbles evolved spanning across two adjacent bins. Swelling was calculated per every single 100-nm bin by the following equation (r_i: the cavity radius, N: the number of cavities, A: the examined area, and t: TEM sample thickness):

$$S\,(\%) = \frac{\sum_{i=1}^{N} \frac{4}{3}\pi r_i^3}{A \times t - \sum_{i=1}^{N} \frac{4}{3}\pi r_i^3} \times 100$$

Error propagation was conducted on measurement concerning the measurement of cavity diameter and swelling. Given a magnification of 110 k in STEM mode, the resolution of STEM images was determined to be 0.8 nm. Consequently, the absolute error in size measurement was estimated as 0.4 nm/pixel, half of unit pixel size. Another error source arises from an inherent 10 % uncertainty associated with the measurement of TEM specimen thickness measurement using EELS [13]. These errors, pertaining to the measurement of cavity size and sample

Table 1
Nominal chemical compositions (wt%) of the tested ferritic/martensitic steels of HT9, Gr.92, FC92–B, and FC92–N.

	HT9	Gr.92	FC92–B	FC92–N
B	–	0.004	0.02	0.01
C	0.21	0.10	0.07	0.07
N	0.006	0.042	0.02	0.08
Si	0.21	0.45	–	–
P	–	0.02	–	–
S	–	0.009	–	–
V	0.33	0.20	0.2	0.2
Cr	11.8	9	9	9
Mn	0.50	0.44	–	–
Fe	Bal.	Bal.	Bal.	Bal.
Ni	0.51	0.042	0.45	0.45
Nb	–	0.072	0.2	0.2
Mo	1.03	0.47	0.5	0.5
Ta	–	–	0.05	0.05
W	0.24	1.6	2	2

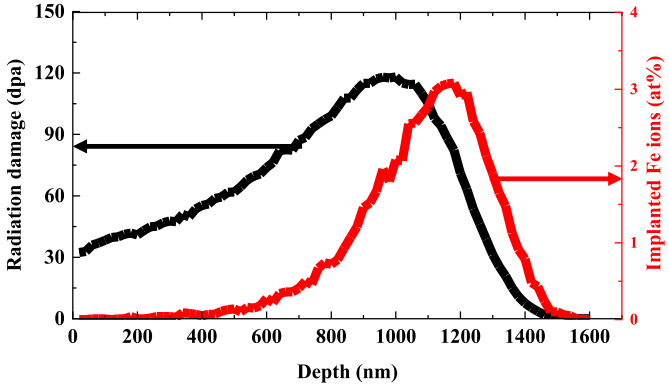

Fig. 1. SRIM-estimated radiation damage (black solid line) and Fe implantation profiles (red solid line) in 3.5 MeV Fe^{++} ion irradiated FC92–B to peak radiation damage of 120 dpa. (For interpretation of the references to colour in this figure legend, the reader is referred to the Web version of this article.)

thickness, were applied to a calculation on swelling.

A visual inspection on the high-angle annular dark field (HAADF) images in Fig. 2–4 reveals that fine and ellipsoidal (or near-spherical) voids and bubbles are present within the first 300 nm of all alloys. This dpa-independent cavity evolution can be attributed to the proximity to the free surface, primarily resulting from the defect imbalance in the near-surface region [14], and/or outward Cr segregation toward the surface [15]. Thus, the midrange depth region of 400–700 nm was chosen to avoid the free surface effects in the near-surface region and injected interstitial effects near the radiation damage peak [16,17].

For the simplicity and brevity in further discussion, a local dpa for the examined 400–700 nm region has been determined by averaging the SRIM-calculation at both ends of 400 and 700 nm depth. The estimated damage between 400 and 700 nm ranges over 58.6–80.5 dpa and 60.0–79.5 dpa for FC92–B and FC92–N, respectively, in cases of peak dose of 120 dpa; 117.2–161.0 dpa, 120.0–159.0 dpa, 116.4–160.8 dpa, and 117.4–160.1 dpa in FC92–B, FC92–N, HT9, and Gr.92, respectively, in cases of peak dose of 240 dpa. As a result, hereinafter, 70 and 140 dpa represents the average dpa in 400–700 nm region for the 120 and 240 peak dpa cases, respectively. The deviation among all combinations of the four alloys and two target damage conditions is found to be less than 1 %.

3. Results

HT9 is composed of tempered martensite with a minor fraction of retained δ-ferrite, whereas the FC92 series and Gr.92 consist solely of fully tempered martensite without any δ-ferrite. Average grain size (ferret diameter) was measured as 9.21 μm for HT9, 7.49 μm for Gr.92, 9.69 μm for FC92–B, and 8.94 μm for FC92–N. Lath lengths ranged from ~600 to 1200 nm and lath widths varied from ~200 to ~700 nm for every tested alloy. Notably, FC92–B exhibited the largest lath structures among the tested alloys. Representative Cr/V-EDS scans, overlaid on with HAADF images from the unirradiated steel alloys, are depicted in the supplementary material (S1). In HT9 and Gr.92, grain boundaries were predominantly adorned with Cr-rich clusters (indicated by yellow arrows in S1), corresponding to $M_{23}C_6$ precipitates formed along the grain boundaries. In contrast, minimal or no Cr or C clusters were observed in the EDS images of the FC92 series. Instead, V-/Nb-rich carbonitrides (indicated by red arrows in S1) were found within the laths

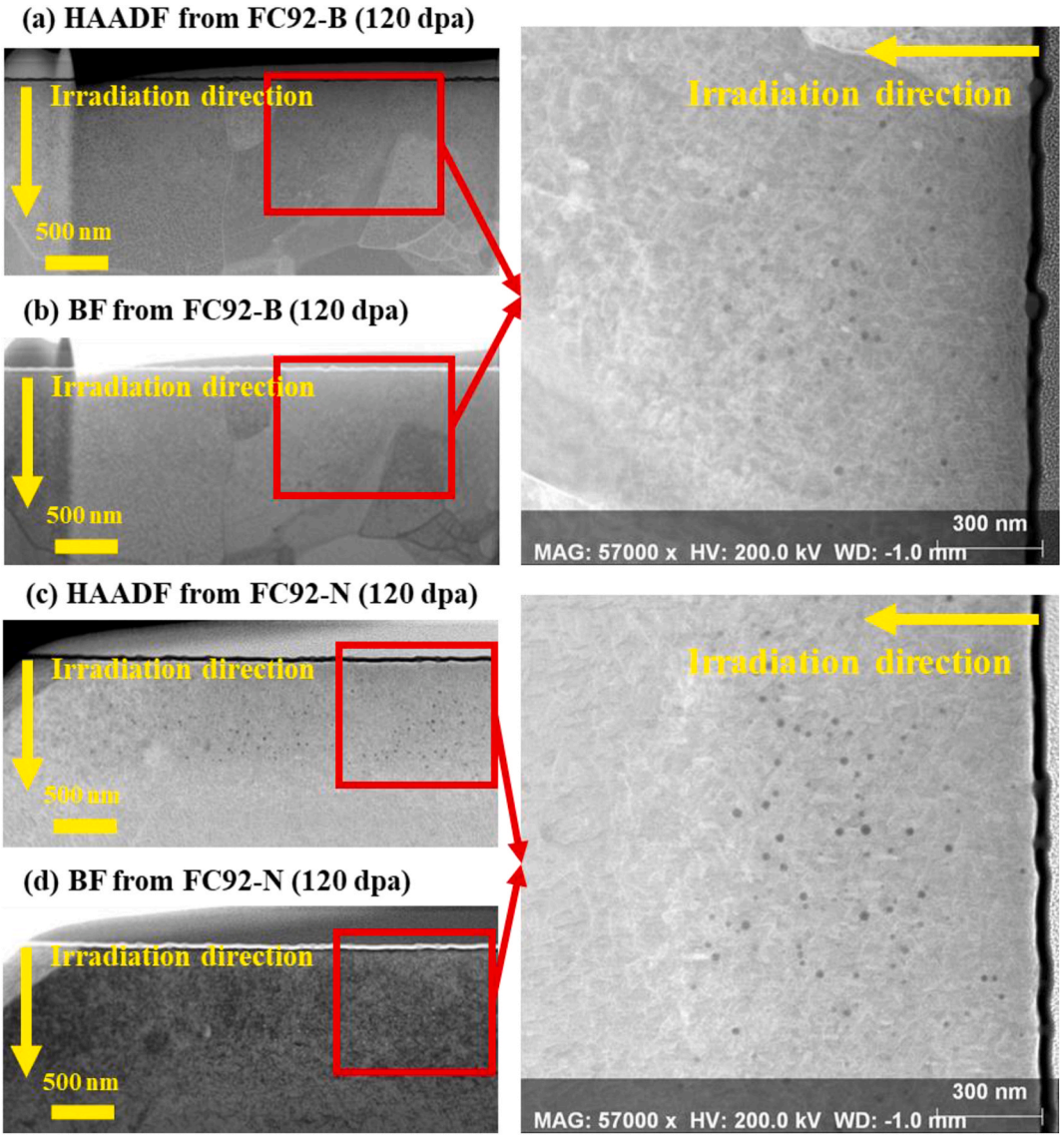

Fig. 2. Low-magnification HAADF and BF images of FC92–B and -N irradiated by 3.5 MeV Fe^{++} ion to 120 dpa/120 appm He at 475 °C (He/dpa ratio: 1 appm/dpa): (a) BF and (b) HAADF obtained from irradiated FC92–B; (c) BF and (d) HAADF obtained from irradiated FC92–N. The irradiation direction in each TEM image is marked with a yellow arrow. (For interpretation of the references to colour in this figure legend, the reader is referred to the Web version of this article.)

of FC92 steel alloys. This phenomenon is likely due to the comparable atomic abundance of B and N, resulting in a uniform distribution of fine-sized $M_{23}C_6$ precipitates along the prior austenite grain boundaries (PAGBs) and MX carbonitrides inside subgrains. B suppresses the coarsening of pre-formed $M_{23}C_6$, while N facilitates MX carbonitride formation. More details regarding the unirradiated microstructures and swelling behaviors at a higher peak radiation damage level of 480 dpa are outlined in our previous study, referenced as Ref. [18].

Fig. 2–4 show cross-sectional BF and HAADF STEM images of 3.5 MeV Fe^{++} ion irradiated steel alloys (Fig. 2: FC92–B and -N irradiated to 120 dpa; Fig. 3: FC92–B and -N irradiated to 240 dpa; Fig. 4: HT9 and Gr.92 irradiated to 240 dpa.) The regions highlighted by red-boxes in each low-magnification image on the left-hand side were further magnified into the higher-magnification (>57 k) HAADF image on the right-hand side. Within the damaged zone of the irradiated steels, numerous small-sized cavities are observed, accompanied by densely-entangled dislocation lines/loops, distinct from unirradiated bulk region. The depth of the radiation-damaged reached 1.5 μm, well matching with the SRIM-expected ion range. Table 2–3 provide the summaries of the examined cavities within the range of 400–700 nm in

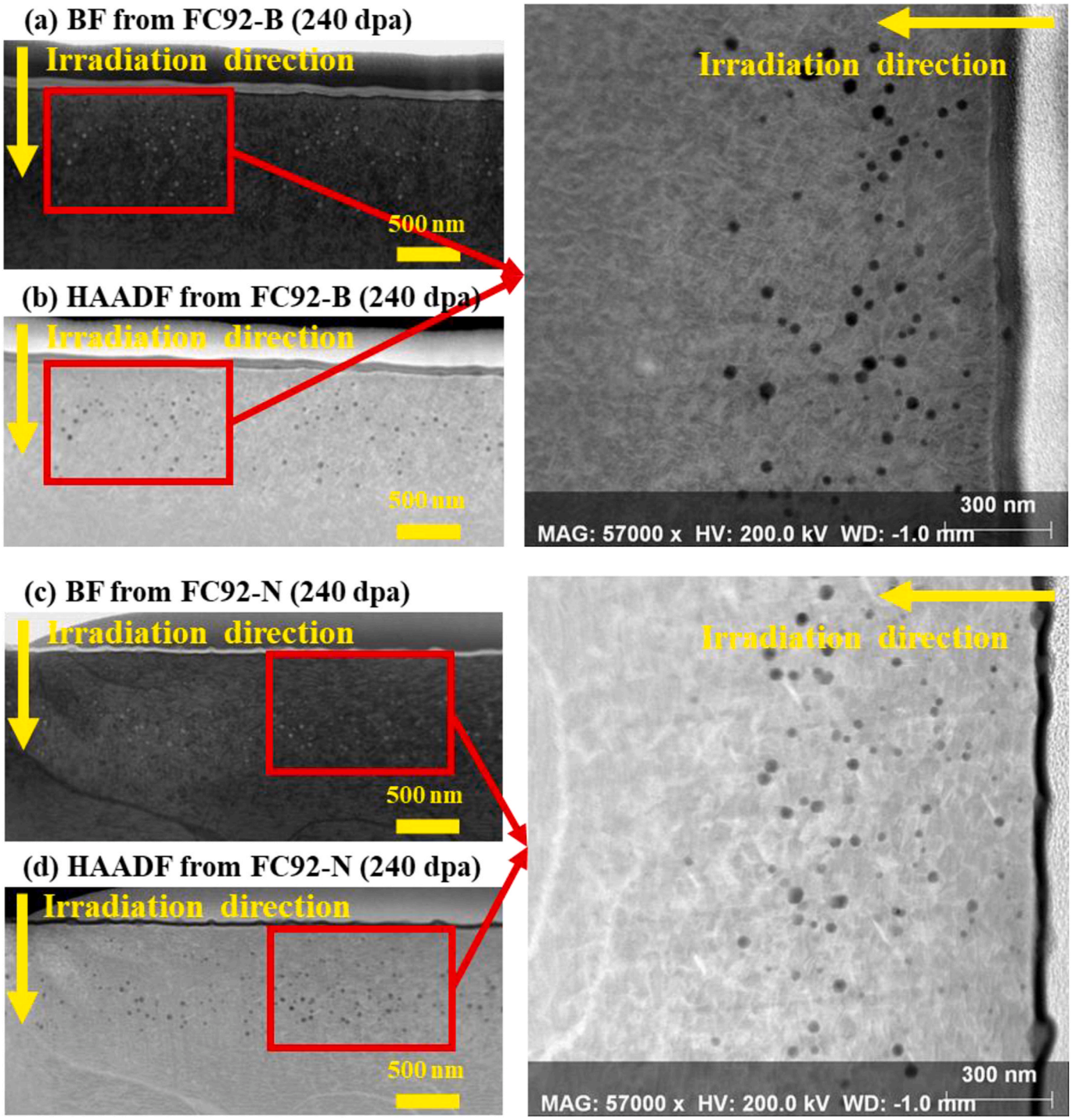

Fig. 3. Low-magnification HAADF and BF images of FC92–B and -N irradiated by 3.5 MeV Fe^{++} ion to 240 dpa/240 appm He at 475 °C (He/dpa ratio: 1 appm/dpa): (a) BF and (b) HAADF obtained from irradiated FC92–B; (c) BF and (d) HAADF obtained from irradiated FC92–N. The irradiation direction in each TEM image is marked with a yellow arrow. (For interpretation of the references to colour in this figure legend, the reader is referred to the Web version of this article.)

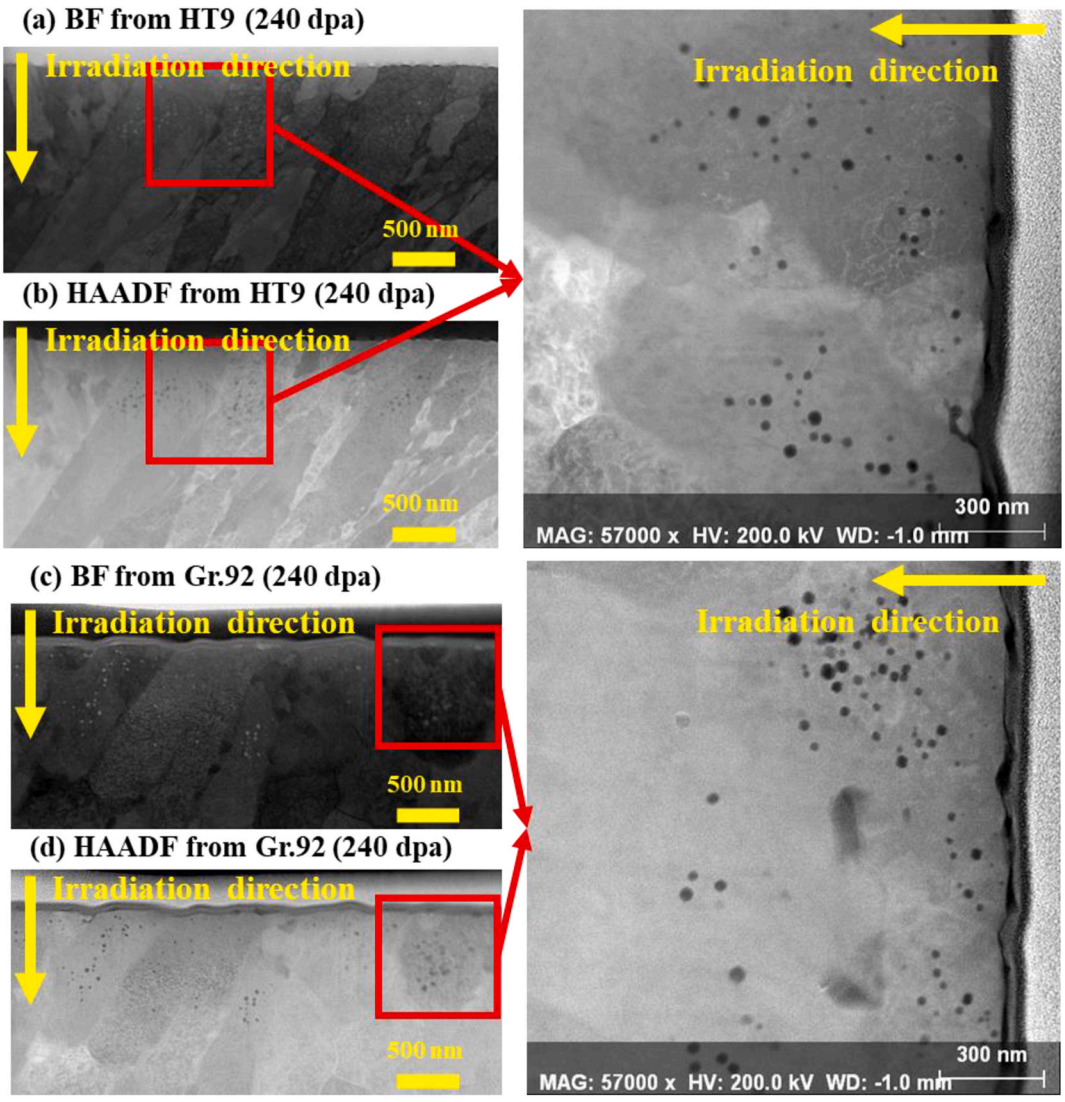

Fig. 4. Low-magnification HAADF and BF images of FC92–B and -N irradiated by 3.5 MeV Fe^{++} ion to 240 dpa/240 appm He at 475 °C (He/dpa ratio: 1 appm/dpa): (a) BF and (b) HAADF obtained from irradiated HT9; (c) BF and (d) HAADF obtained from irradiated Gr.92. The irradiation direction in each TEM image is marked with a yellow arrow. (For interpretation of the references to colour in this figure legend, the reader is referred to the Web version of this article.)

Table 2
Summary of cavities observed in 400–700 nm depth region (dpa level: 70 dpa, pre-implanted helium level: 70 appm) of FC92 steels irradiated by 3.5 MeV Fe^{++} ion up to 120 dpa with He implantation of 1 appm/dpa.

Alloy		FC92–B	FC92–N
Number of voids & bubbles (the entire examined area, μm²)		246 (2.02)	149 (1.88)
Swelling (%) over the entire damaged area		1.0	0.5
Number of cavities in 100 nm bins (400–700 nm)	**400–500**	26	27
	500–600	30	28
	600–700	30	19
Void and bubble number density (10^{20}/m³) in 400–700 nm depth region		18.8	16.9
Average diameter (nm) of void & bubbles in 400–700 nm depth region		19.9	18.2
Swelling (%) in 400–700 nm depth region		1.1	0.8

Table 3
Summary of cavities observed in 400–700 nm depth region (dpa level: 140 dpa, pre-implanted helium level: 140 appm) of F/M steels irradiated by 3.5 MeV Fe^{++} ion up to 240 dpa with He implantation of 1 appm/dpa.

Alloy		HT9	Gr.92	FC92–B	FC92–N
Number of voids & bubbles (the examined area, μm²)		162 (0.99)	101 (0.73)	79 (1.83)	128 (1.83)
Swelling (%) over the entire damaged area		3.9	2.7	1.4	2.0
Number of cavities in 100 nm bins (400–700 nm)	**400–500**	13	38	16	13
	500–600	16	38	12	9
	600–700	18	31	9	14
Void and bubble number density (10^{20}/m³) in 400–700 nm depth region		21.2	39.8	8.7	11.6
Average diameter (nm) of void & bubbles in 400–700 nm depth region		32.7	24.6	34.3	33.6
Swelling (%) in 400–700 nm depth region		7.4	6.3	2.9	3.6

the irradiated steels: Table 2 details swelling characterization in FC92 steels at 70 dpa/70 appm He; Table 3 outlines swelling characterization in HT9, Gr.92, FC92–B, and FC92–N at 140 dpa/140 appm He.

3.1. Cavity evolution in FC92 steels at 70 and 140 dpa

Fig. 5a shows cavity number density distribution in the FC92–B and -N irradiated to 120 and 240 dpa as a function of depth. All four combinations of two alloys/two doses exhibited similarity in their bimodal number density distribution. In the first 0–300 nm region, all cases exhibited a large population of small-sized cavities. This dpa-insensitive cavity evolution in the near-surface region can be an artifact from the defect imbalance from forward scattering along the ion path [14,19]. After 300 nm, the number density continuously increased to its peak, followed by a gradual decrease towards the observed depth's end. This reflects the injected interstitial effect near the radiation damage peak at ~1000 nm. Across the examined range of 400–700 nm, at least 50 % higher cavity population was observed at 70 dpa compared to 140 dpa for both FC92 alloys. Alloy-by-alloy comparison at two given dpa conditions demonstrates a higher number density in FC92–B than in FC92–N at 70 dpa. However, at 140 dpa, FC92–N showed a higher number density than FC92–B. Thus, a clear conclusion regarding comparative ability of the two FC92 steels in suppressing cavity nucleation cannot be drawn from these findings.

Fig. 5b plots the average cavity diameter distribution in FC92 alloys as a function of depth. Both FC92 alloys showed similar trends in their size distributions. The observed diameter showed a steady increase, reaching a peak at ~600–800 nm before decreasing. Between 400 and 700 nm, larger-sized cavities were found at 140 dpa than at 70 dpa. Across all alloy types, an increase in dose from 70 to 140 dpa yielded a nearly a twofold increase in the maximum and average cavity sizes. Specifically, the maximum in size measured was 35.8 nm for FC92–B and 64.2 nm for FC92–N at 70 dpa, while it increased to 64.2 nm FC92-Bfor FC92–N, it was 32.5 nm at 70 dpa and 59.2 nm at 140 dpa. Average size of the examined diameters within the 400–700 nm range was 20.2 nm at 70 dpa and 34.3 nm at 140 dpa for FC92–B; 17.2 nm at 70 dpa and 33.6 nm at 140 dpa for FC92–N, respectively. Notably, FC92–B exhibited slightly larger cavity size than FC92–N for both 70 and 140 dpa conditions. Normalized cavity size distributions in FC92 alloys at 70 and 140 dpa are presented in Fig. 6. For both alloys, the most prevalent voids had medial sizes for both dose conditions. The size distributions at 140 dpa were centered at larger diameters than those of 70 dpa, reflecting the larger average diameters at 140 dpa. Some large-sized cavities of >50 nmD were exclusively found at 140 dpa, indicating more active cavity growth at higher dose of 140 dpa. However, the coexistence of small-sized cavities (<10 nmD) even at a low ratio indicates that there still has been a weak cavity nucleation.

Fig. 7 plots a depth-dependent swelling distribution over the entire damaged region in the FC92 alloys irradiated to two peak doses of 120 and 240 dpa. All steels exhibited unimodal swelling curves, resembling

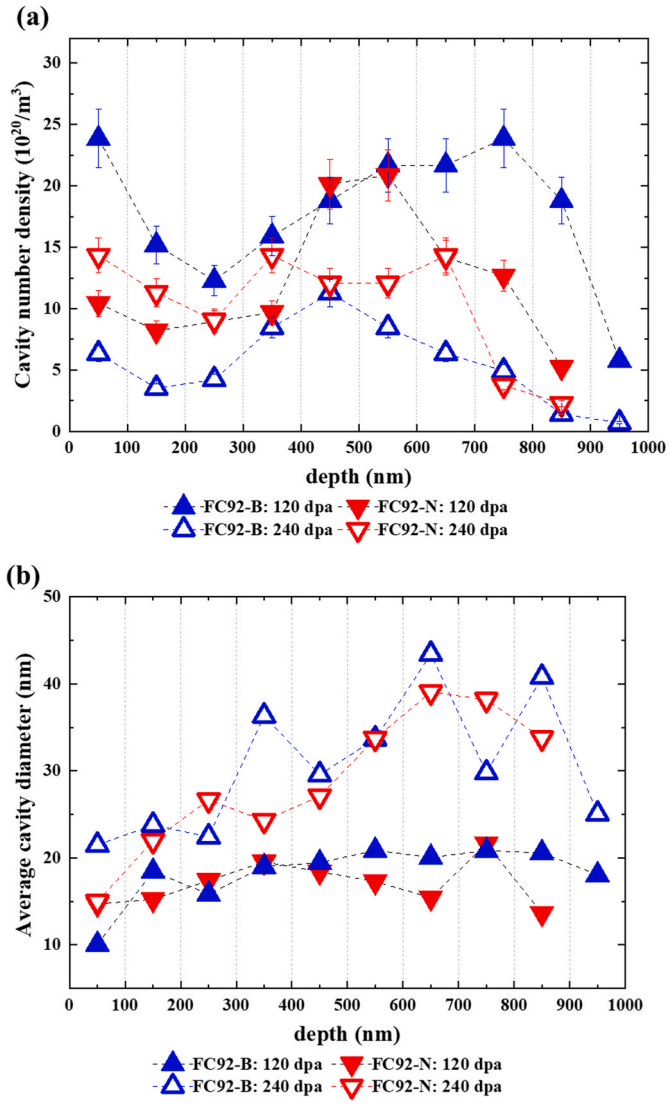

Fig. 5. Depth-dependent cavity (a) number density and (b) size distribution in FC92 steels under 3.5 MeV Fe^{++} ion irradiation to the peak dose of 120 and 240 dpa at 475 °C (He/dpa ratio: 1 appm/dpa.).

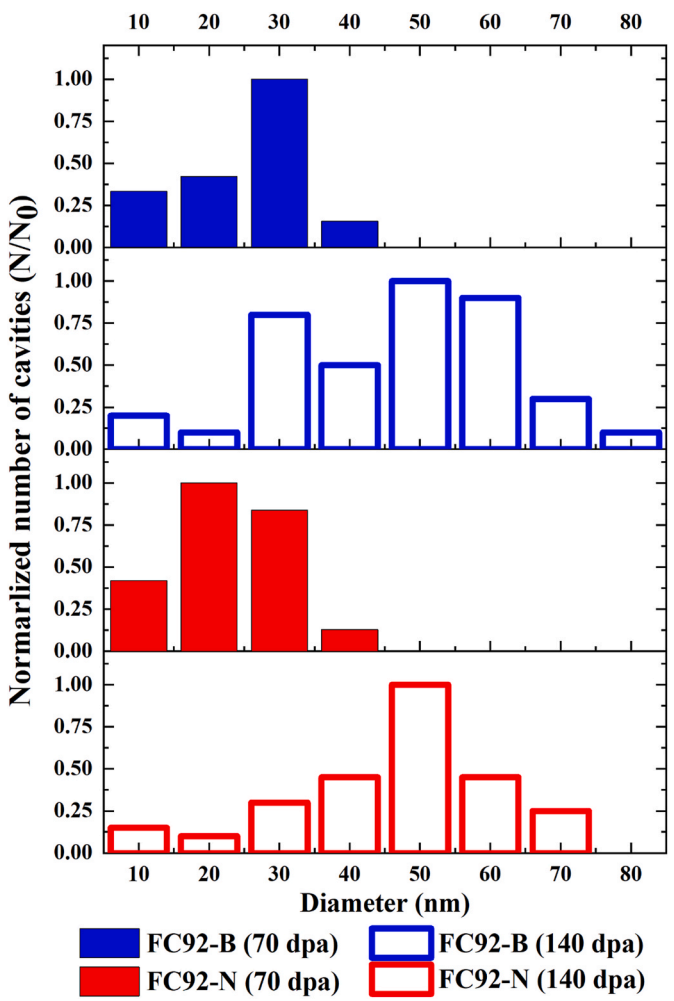

Fig. 6. Normalized cavity size distribution in 3.5 MeV Fe^{++} ion irradiated FC92 steels at 70 and 140 dpa (He/dpa ratio: 1 appm/dpa, irradiation temperature: 475 °C.).

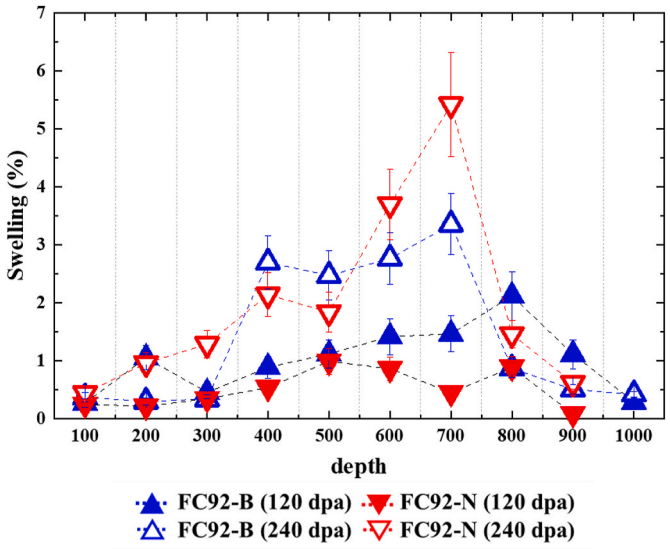

Fig. 7. Swelling profiles in 3.5 MeV Fe^{++} ion irradiated FC92 steels at the peak radiation damage condition of 120 and 240 dpa with 120 and 240 appm He, respectively (He/dpa ratio: 1 appm/dpa, irradiation temperature: 475 °C.).

the SRIM-estimated radiation damage profile but with a shift toward the surface. Swelling monotonically increased from the surface, reaching its maximum at the 700–900 nm region, followed by a decrease. Fig. 8 compares the swelling of the irradiated F/M steels at 70 and 140 dpa. At 70 dpa, FC92–N less swelled than FC92–B as swelling reached 1.3 % in FC92–B and 0.8 % in FC92–N. The lower swelling in FC92–N at 70 dpa can be attributed to both suppressed cavity nucleation and growth. Conversely, at 140 dpa, FC92–B less swelled than FC92–N with swelling of 2.9 % in FC92–B and 3.6 % in FC92–N. This lower swelling in FC92–B at 140 dpa primarily stems from a lower cavity number density, as the difference in average cavity diameter between two alloys remained less than 1 nm. Both FC92 alloys exhibited higher volumetric swelling at 140 dpa compared to 70 dpa. The higher degree of swelling observed at 140 dpa for both FC92 alloys, despite the lower cavity number density, suggests that swelling at given dose condition primarily depends on cavity growth rather than nucleation. In other words, radiation resistance of the FC92 series has been shifted from being influenced by cavity nucleation to being driven by growth, supported by a very weak cavity nucleation at 140 dpa from Fig. 14.

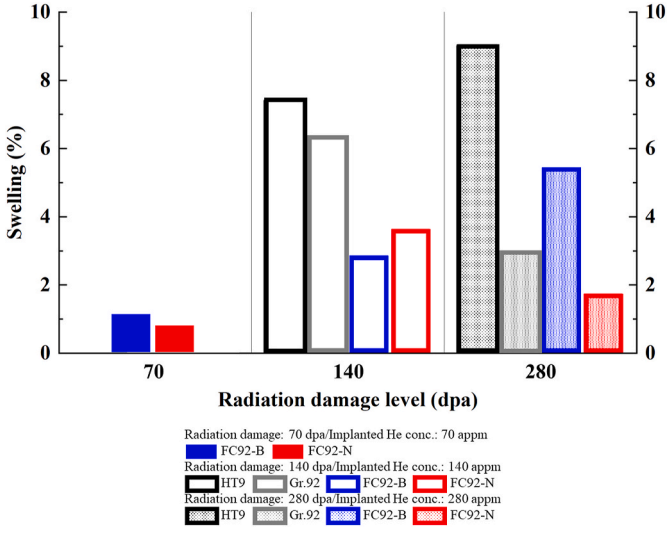

Fig. 8. A comparison in the swelling of 3.5 MeV Fe^{++} ion irradiated steels at 70, 140, and 280 dpa with 70, 120 and 240 appm He, respectively (He/dpa ratio: 1 appm/dpa, irradiation temperature: 475 °C.).

3.2. Cavity evolution in the irradiated four F/M steels at 140 dpa

Fig. 9a shows the cavity number density distribution in the two FC92 series and two reference alloys irradiated to a peak damage of 240 dpa. All four alloys displayed similar bimodal patterns in their density distributions, although the density peaks occurred at different depths among the alloys. In the near-surface region (0–400 nm), a large population of cavities was observed, marking their first density peak. After the first 400 nm depth, all alloys exhibited an increase in number density, leading to the second peak observed at 700–800 nm in HT9, 500–600 nm in Gr.92, 400–500 nm in FC92–B, and 600–700 nm in FC92–N. Notably, FC92 steel alloys demonstrated lower density than HT9 and Gr.92 throughout the entire irradiated region. Between 400 and 700 nm, Gr.92 had the largest number density of cavities, containing over double the number of cavities observed in HT9. HT9 followed with the second largest density, nearly twice those of FC92 series.

Fig. 9b plots the cavity average diameter distribution in the four alloys irradiated to 240 dpa versus a depth. Cavity sizes increased from

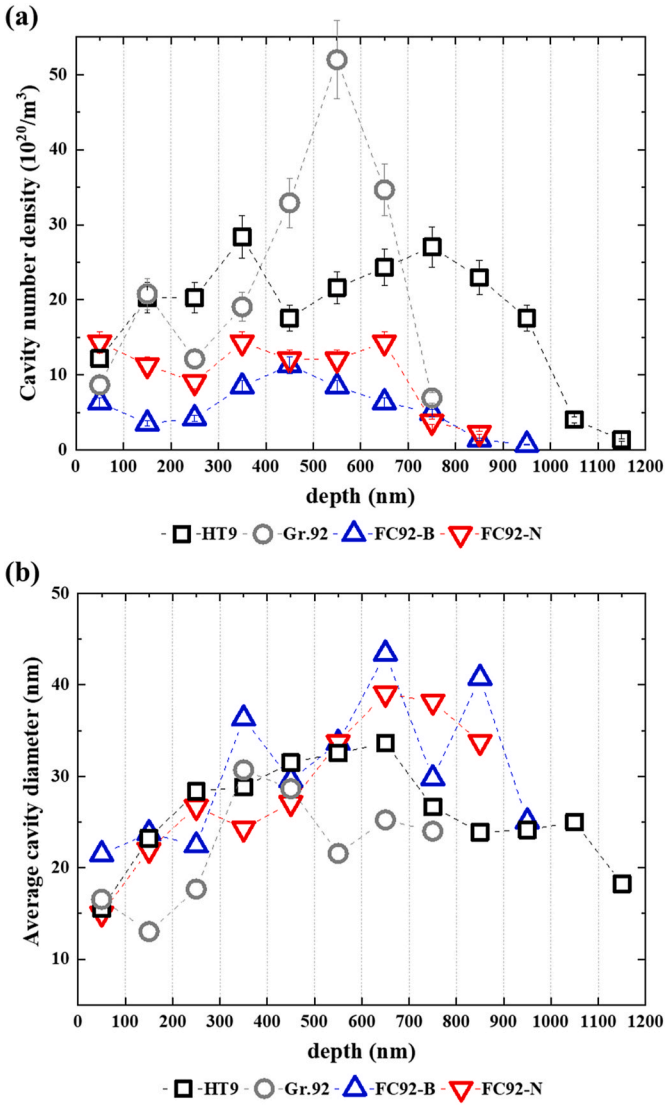

Fig. 9. Depth-dependent cavity (a) number density and (b) size distribution in the tested steels under 3.5 MeV Fe^{++} ion irradiation at 475 °C (target damage: 240 dpa, He/dpa ratio: 1 appm/dpa.).

the surface to the alloys' peaks at differential depth bins: 600–700 nm in HT9, 300–400 nm in Gr.92, 700–800 nm in FC92–B, and 700–800 nm in FC92–N. After that, the average size continuously decreased in all four alloys. Within the 400–700 nm region, the maximum cavity size was measured as 79.6 nm in HT9, 74.3 nm in Gr.92, 64.2 nm in FC92–B, and 59.2 nm in FC92–N; the average size was 32.7 nm in HT9, 24.6 nm in Gr.92, 34.3 nm in FC92–B and 33.6 nm in FC92–N. On average, FC92 steels had higher size than the other two reference steels. However, it is noteworthy that both HT9 and Gr.92 steels exhibited maximum diameters exceeding those of FC92 steels by more than 10 nm. Cavity size distributions between 400 and 700 nm of irradiated steels are normalized in Fig. 10. All tested alloys exhibited similar size distributions in the form of a typical Gaussian distribution. Some voids in HT9 and Gr.92 exhibited diameter far from the average, indicating more progressed growth behavior. The majority of cavities in HT9 and FC92 steels were centered around diameters of 50–60 nm with a sparse population of small-sized cavities having a diameter of <10 nm. Gr.92 exhibited a relatively higher abundance of small-sized cavities of <10 nmD. However, as depicted in Fig. 14, most of cavities in the small-sized group were already sized above 4 nm in radius. Considering the critical radius is approximately estimated at 2 nm in ion-irradiated F/M steels, this implies that Gr.92 already exhibited a mature growth-dominated cavity behaviors over nucleation, similar to the other three alloys, supported by a tail at higher diameters exceeding 40 nm.

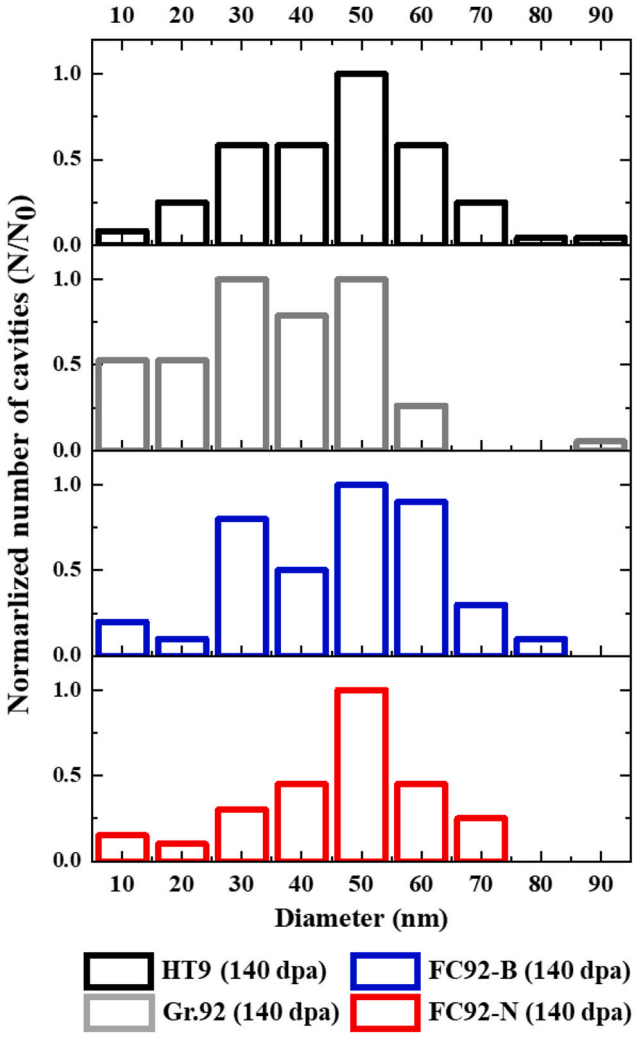

Fig. 10. Normalized cavity size distribution in 3.5 MeV Fe^{++} ion irradiated ferritic/martensitic steels at 140 dpa (implanted He/dpa ratio: 1 appm/dpa, irradiation temperature: 475 °C.).

Swelling in the four alloys irradiated to 240 dpa is provided as a function of depth in Fig. 11. All steels exhibited unimodal swelling profiles over the irradiated region. The entire swelling observed across the damaged region was attained as 3.9 % in HT9, 2.7 % in Gr.92, 1.4 % in FC92–B, and 2.0 % in FC92–N; whereas the swelling within 400–700 nm depth region reached as 7.4 % in HT9, 6.3 % in Gr.92, 2.9 % in FC92–B, and 3.6 % in FC92–N. Between 400 and 700 nm, HT9 and Gr.92 swelled almost twice or more as compared to FC92 alloys. This higher swelling in two reference steels can be attributed to higher cavity number density as well as a few larger-sized cavities measuring over 80 nmD. This is because HT9 and Gr.92 had similar (or slightly smaller) average cavity size to FC92 series over the examined region. Consequently, it can be inferred that the swelling resistance between alloys still predominantly relies on the suppression of cavity nucleation while also exhibiting some dependence on cavity growth. While the grain size of alloy Gr.92 and FC92–N remains smaller compared to other alloys, no clear correlation with swelling results has yet been found. Previous studies reported that the introduction of MX precipitates can indeed increase high-temperature creep resistance [20,21], and some have suggested that MX precipitate may also serve as effective defect annihilation sites [22]. Therefore, one plausible interpretation is that MX precipitates within lath structure of the FC92 alloys may help suppress swelling. However, definite experimental evidence is still lacking regarding the sink strength of MX precipitate and coherency of this kind of precipitate within the matrix. Thus, further research is essential to explore the efficacy of the precipitate/matrix interface in MX precipitates in enhancing irradiation resistance, given that swelling is determined by a confluence of various microstructural characteristics, including but not limited to grain size and MX precipitates.

4. Discussion

4.1. A comparison in swelling behaviors of the four steels between at 140 and 280 dpa

Cavity evolution in the HT9, Gr.92, FC92–B, and FC92–N at 140 dpa is compared to swelling data at 480 peak dpa from Ref. [18]. Both ion-irradiation experiments were conducted on the same four alloys under identical beam-irradiating conditions, encompassing factors such as ion source, beam flux/energy/type, He/dpa ratio, and temperature. The only differences between the two studies were the total ion fluence and implanted helium concentration. To determine a local dpa for the 400–700 nm region in F/M steels irradiated to the peak 480 dpa, a

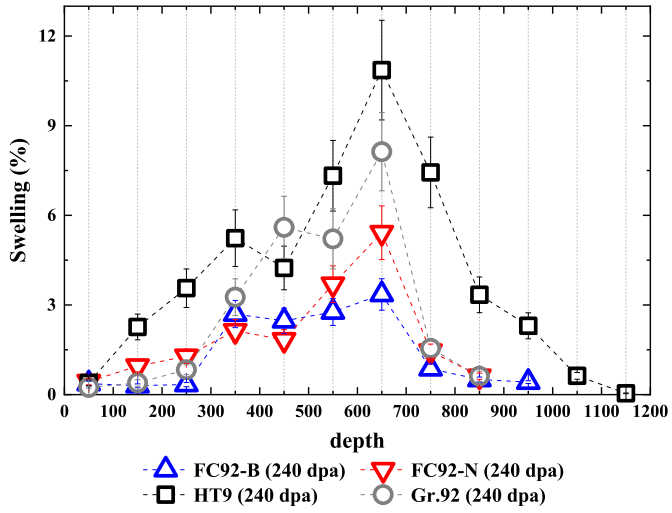

Fig. 11. Depth-dependent swelling distribution in 3.5 MeV Fe^{++} ion irradiated ferritic/martensitic steels (Peak radiation damage: 240 dpa, implanted He/dpa ratio: 1 appm/dpa, irradiation temperature: 475 °C.).

method described in section 2.2 was employed. For this midrange region in the four steels irradiated to 480 dpa, radiation damage falls within a range of approximately 235–320 dpa, with a deviation of less than 3 % among the alloys. Thus, the pre-implanted helium content also ranges from 235 to 320 appm. This estimation resulted in a calculated dose of 280 dpa, with corresponding implanted helium contents of 280 appm.

Fig. 12 presents a comparison of the average diameter and number density of cavities at 140 dpa, along with those observed at 280 dpa. At 140 dpa, average cavity diameter for HT9, Gr.92, FC92–B, and FC92–N was measured as 32.7 nm, 24.6 nm, 34.3 nm, and 33.6 nm at 140 dpa. Comparatively, at 280 dpa, the average diameters increased to 48.8 nm, 33.5 nm, 40.0 nm, and 36.0 nm, respectively. The difference in average cavity diameter between 140 and 280 dpa ranged from 2.4 nm for FC92–N to 16.1 nm for HT9, indicating a more pronounced cavity growth at the higher dose of 280 dpa. Cavity density for all alloys irradiated at 140 dpa/140 appm He, with the exception of FC92–B, was higher than that observed at 280 dpa/280 appm He. In both HT9 and FC92–N, the number density was almost 50 % higher at 140 dpa compared to 280 dpa, whereas in FC92–N, it was 10 % higher at 140 dpa. Only FC92–B had an increase in number density from 140 to 280 dpa. Overall, an increase in dose resulted in an increase in size and a decrease in number density.

Fig. 13 compares the normalized cavity size distribution between 140 and 280 dpa. Among the cases, only Gr.92 and FC92–N at 280 dpa/280 appm He developed a bimodal cavity size distribution, characterized by a relevant abundance of small-sized (<10 nmD) cavities. Conversely, the other cases all followed the Gaussian-like unimodal distribution, regardless of radiation damage. Fig. 14 provides a more detailed comparison of the normalized size distribution of cavities with a radius smaller than 10 nm. It is important to highlight that Gr.92 and FC92–N at 280 dpa/280 appm He exhibited fundametally different cavity behaviors by forming very small-sized cavities with radii of <2 nm, distinct from other alloy/dpa (or helium contents) combinations. In HT9, Gr.92, and FC92–N at 280 dpa, over half of small-sized cavity groups (<10 nmD) were sized below 2 nm. In contrast, other doses or alloys predominantly exhibited cavity radii exceeding 5 nm, with very few cavities below 2 nm. While this study does not involve specific calculations related to the critical radius based on the chemical compositions and irradiating parameters, generally, the critical radius of cavities in irradiated ferritic/martensitic steels remains within the range of tenths to 10 nm. Thus, critical radius of 2 nm was chosen in this study, based on the theoretical estimates of ~1.9 nm by Monterrosa [23] and ~2 nm by Hishinuma and Mansur [24], as well as experimentally-measured result of ~2.5 nm by Holton [25]. As evidenced from Figs. 13 and 14, it can be inferred that a significant amount of cavities in Gr.92 and FC92–N at 280 dpa were sized around (or below) critical radius. Meanwhile, the small-sized cavities in HT9 appeared to have little to no significance on swelling behavior at 240 dpa due to their very small proportion compared to the overall examined cavities. Therefore, all the combinations, except Gr.92 and FC92–N at 280 dpa/280 appm He, display cavity behavior of which most of cavities exceed a critical size for continuous growth.

Fig. 8 presents a comparison of the swelling behavior at 140 dpa/140 appm He in HT9, Gr.92, FC92–B, and FC92–N with that at 280 dpa/280 appm He. The volumetric swelling in the four alloys at 280 dpa/280 appm He is referred as 9.0 % for HT9, 2.9 % for Gr.92, 5.4 % for FC92–B, and 1.7 % for FC92–N; that at 140 dpa/140 appm was 7.4 % in HT9, 6.3 % in Gr.92, 2.9 % in FC92–B, and 3.6 % in FC92–N. A comparison of swelling levels between 140 and 280 dpa reveals noteworthy distinctions: FC92–N and Gr.92 exhibited greater swelling at the lower dose of 140 dpa/140 appm He, while HT9 and FC92–B displayed higher swelling levels at the higher dose of 280 dpa/280 appm He. As noted above, all alloys consistently demonstrated an increase in average size and a decrease in number density with the dose increment of 140 dpa, except for the observed increase in number density observed in FC92–B. Thus, this increase in average size primarily contributes to an increase in swelling in HT9; while in the case of FC92–B, both increases in number density and size concurrently acted as contributing factors to the increase in swelling. Conversely, despite exhibiting similar cavity behavior to HT9, the Gr.92 and FC92–N group experienced a reduction in swelling with an increasing dose. This reduction is attributed, as shown in Figs. 13 and 14, to a substantial proportion of the examined

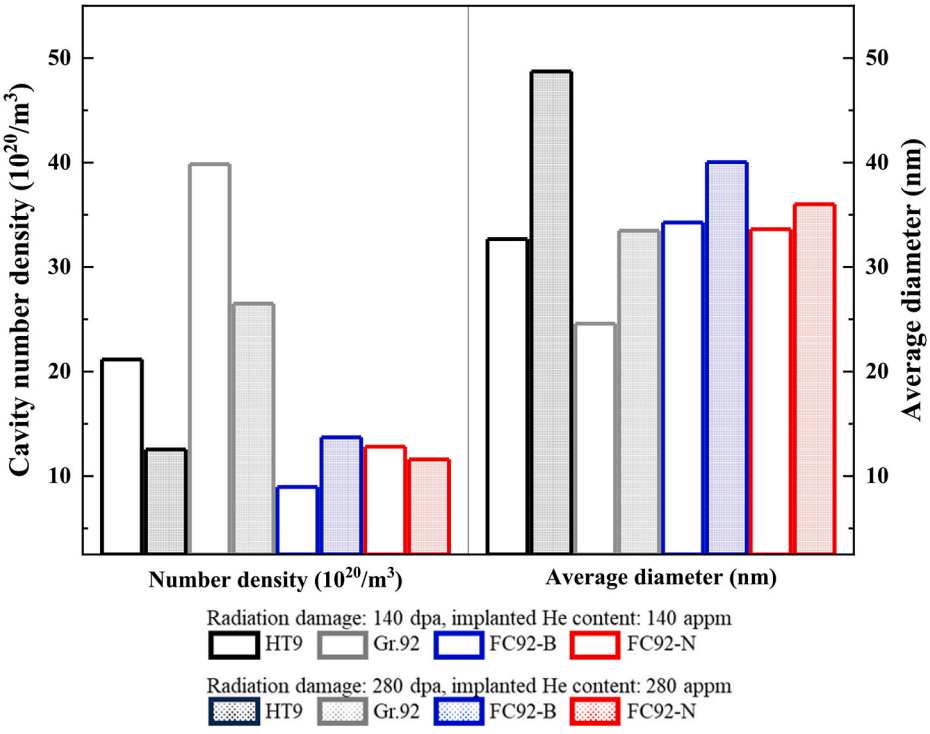

Fig. 12. A comparison in cavity evolution in 3.5 MeV Fe^{++} ion irradiated ferritic/martensitic steels between 140 dpa/140 appm He condition from this study and 280 dpa/280 appm He condition from Ref. [18] (irradiation temperature: 475 °C.).

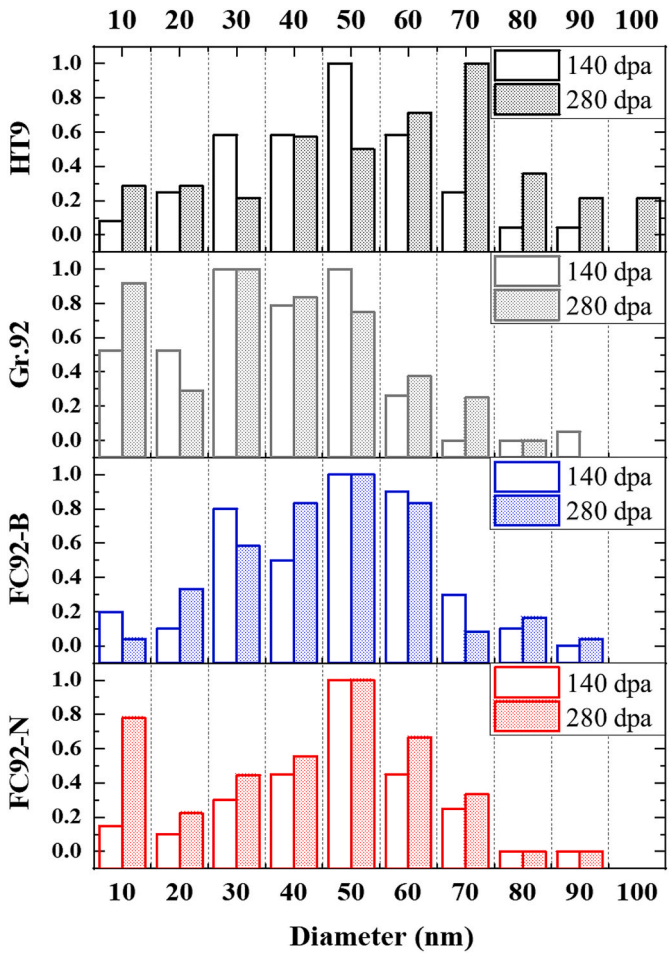

Fig. 13. A comparison in normalized cavity size distribution between 140 dpa/140 appm He and 280 dpa/280 appm He from 3.5 MeV Fe^{++} ion irradiated ferritic/martensitic steels: the empty bar indicates 140 dpa/140 appm He condition from this study, while dotted bar indicates 280 dpa/280 appm He condition from Ref. [18] (irradiation temperature: 475 °C.).

cavities consisting mainly of small voids with a radius below 2 nm.

4.2. The occurrence of a bimodal cavity size distribution in Gr.92 and FC92–N at 280 dpa/280 appm He

A bimodal size distribution was exclusively found in Gr.92 and FC92–N at 280 dpa/280 appm He. The gas-associated bimodal size distribution typically refers to a combined observation of two cavity groups: (1) a dense concentration of gas-stabilized cavities at small sizes below (or around) critical radius, which do not grow with increasing irradiation dose, and (2) another population showing bias-driven growth at larger sizes, with only a restricted number of cavities found between two groups [24]. Early theoretical work by Hishinuma and Mansur on critical radius and bimodal cavity size distribution posited that an appearance of bimodal distribution must align a reduction in critical radius in the presence of helium [24]. In a self-ion irradiation study on T91 irradiated to 356 dpa by Monterrosa [23], the presence of a bimodal cavity size distribution was solely observed in high helium content levels of 100 and 1000 appm He, coinciding with suppressed swelling compared to their counterparts with lower helium levels of 0, 1, and 10 appm. After conducting a simulation study based on Hishinuma and Mansur's theory, Monterossa suggested a range of ~50–400 He/cavity as a pratcial threshold to form a bimodal distribution. Most recently, Lin investigated void and bubble evolution in 8-MeV Ni^{3+} ion irradiated Fe and Fe–3Cr/-10Cr/-14Cr ferritic alloys to 30 dpa with two

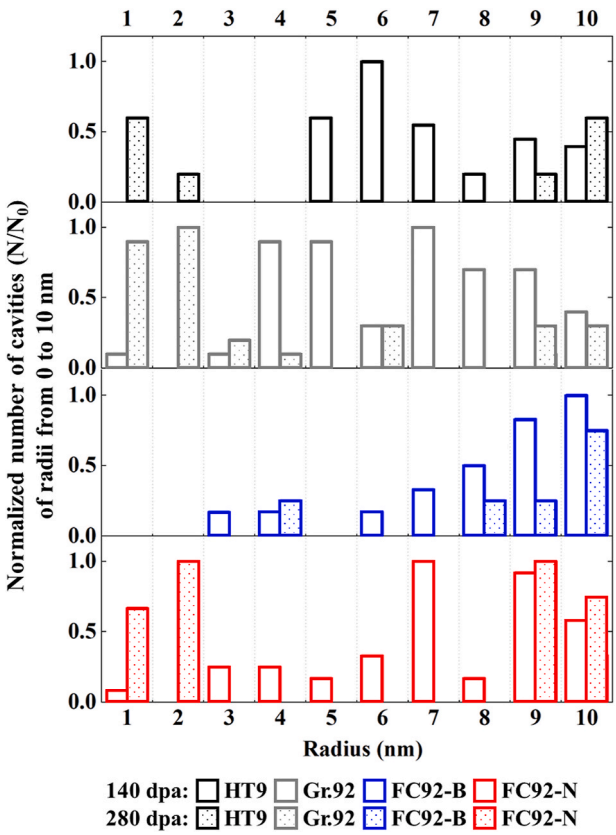

Fig. 14. A comparison in normalized size distribution of the small-sized cavities (radius: 1–10 nm) in 3.5 MeV irradiated ferritic/martensitic steels: the empty bar indicates 140 dpa/140 appm He condition from this study; while the dotted bar indicates 280 dpa/280 appm He condition from Ref. [18] (irradiation temperature: 475 °C.).

different He/dpa ratio of 0.1 and 10 appm He/dpa at varying temperatures from 400 to 550 °C [26]. A bimodal size distribution was observed at temperature above 470 °C in the case of 10 appm He/dpa, regardless of chromium content, but was absent in 0.1 appm He/dpa. In a further detailed analysis on Fe and Fe–10Cr ferritic alloys at 30 dpa/500 °C with He implantation rates of 0.1, 10, and 50 appm He/dpa [27], Lin showed that the size of void-like cavities (<2 nm) decreased with increasing He/dpa, while that of bubble-like (>2 nm) cavities remained constant. Notably, only voids were observed for 0.1 appm He/dpa. As a result, a bimodal size distribution was observed in 10 and 50 appm He/dpa cases for Fe and Fe–10Cr alloys, but not found in 0.1 appm He/dpa cases. In summary, as elucidated in the above-mentioned literature, it can be inferred that the occurrence of a bimodal size distribution is unequivocally dependent on the quantity of helium and is observed only under conditions of relatively high helium content.

A bimodal size distribution, characterized by a prevalence of small-sized cavities in Gr.92 and FC92–N at 280 dpa/280 appm He, may signify a prolonged duration of the incubation/transient regime [28,29]. This indicates a delayed shift occurred in Gr.92 and FC92–N from a stage primilary governed by cavity nucleation to one where cavity growth takes precedence. In contrast, other combinations in dose/alloy combinations had already transitioned towards a stage where mature cavity growth predominates over nucleation, significantly surpassing a critical radius of around 2 nm. However, any overstatement in the alloy-specific details on the material chemistry should be avoided here, as HT9 and FC92–B exhibited mature growth behavior, and swelling data still remains inadequate to explain this differential response by alloys.

4.3. The effect of pre-implanted helium on swelling suppression

Gr.92 and FC92–N exhibit a negative correlation between dose and swelling, wherein higher degree of swelling occurred at lower dose of 140 dpa/140 appm He compared to 280 dpa/280 appm He. This finding suggests a potential swelling suppression at higher dose of 280 dpa/280 appm He. Previous experimental studies have highlighted that introducing insoluble gas atoms before/during irradiation often suppresses swelling in ion-irradiated metals and alloys [15,23,30]. The implanted helium atoms, due to their strong binding energy to vacancies, primarily stabilize vacancy clusters, serving as the nucleation sites for voids [31,32]. According to theory, these helium-stabilized vacancy clusters fail to reach the critical radius for continuous growth, thereby enhancing early cavity nucleation and impeding the growth of cavities formed earlier, consequently suppressing swelling [29]. An early study by Farrell et al. investigated the effect of helium implantation on swelling using three different helium injection modes: no helium, helium pre-injection, and helium co-injection [30]. Irradiation was conducted utilizing 4 MeV Ni^{++} ions on 17Cr–17Ni-2.5Mo austenitic alloy at 625 °C, reaching a dose of 70 dpa. Helium pre-implantation delayed the growth of void diameter, facilitating increased number density and less swelling compared to the other two cases. Farrell postulated that the inhibited swelling behavior in the helium pre-implanted case likely resulted from early nucleation/stabilization of the voids, preventing them from reaching a size sufficient to act as a biased sink for adjacent vacancies. Recent experimental approaches have systematically explored the effect of implanted helium atoms on cavity evolution at high radiation damage levels. Getto compared swelling behaviors in 5-MeV self-ion irradiated HT9 up to 375 dpa between pre-implanted helium contents of 0, 1, 10, and 100 appm across a broad temperature range of 400–480 °C [15]. At 440 °C and 188 dpa, an increasing helium content from 10 appm He to 100 appm He resulted in increased void number density and decreased diameter. Consequently, HT9 swelled to 0.13 % at 100 appm He, which is lower than 0.22 % at 10 appm He. Getto attributed this suppressed swelling at high helium contents to helium-assisted early stabilization of voids, which resulted in a promotion in void nucleation and inhibition in the growth of nucleated cavities, in accordance with Farrell's findings. Monterrosa conducted a comparative study on swelling evolution in 5.0 and 4.4 MeV Fe^{++} ion irradiated T91 steels to 350 dpa at pre-implanted helium levels of 0, 1, 10, 100, and 1000 appm [23]. Between 45 and 356 dpa, a consistent trend was found in cavity behaviors, where an increase in helium contents led to a reduction in cavity size and an increase in density. At 300 dpa, swelling reached at least 2.7 % for 0–10 appm cases, while remaining below 0.61 % for 100 and 1000 appm cases. Similarly, at 365 dpa, swelling reached at least 3.5 % for lower helium levels of 0–10 appm cases, compared to only 0.78 % and 0.15 % for 100 and 1000 appm cases, respectively. Monterrosa proposed that helium trapping and/or alteration of cavity and dislocation bias likely contribute to the suppression in swelling at high helium levels exceeding 100 appm, based on sink strength calculation from cavities and dislocations. Furthermore, Lin conducted a comparative study on Fe and Fe–10Cr ferritic alloys dual-beam irradiated (8 MeV Ni^{3+} and 3.5 MeV He^{2+}) to 30 dpa with He implantation rates of 0.1, 10, and 50 appm He/dpa at 500 °C [27]. As the helium production rate increased from 0.1 to 50 appm/dpa, cavity size decreased by ~60 %, while the density peaked at intermediate 10 appm/dpa. As a result, swelling peaked at 10 appm/dpa, approximating helium content between 300 and 400 appm. These studies collectively demonstrate that the addition of helium exceeding 100 appm tends to suppress swelling by triggering less cavity growth as well as higher cavity number density.

Thus, one plausible conclusion can be made here: an excess amount of pre-implanted helium exceeding 200 appm can be the primary factor contributing to the suppressed swelling in Gr.92 and FC92–N at higher dose of 280 dpa. The distinctive occurrence of a bimodal size distribution further supports the interpretation of helium-associated swelling suppression in Gr.92 and FC92–N. While a bimodal size distribution is not always inherent to the suppression of swelling, ongoing cavity nucleation in Gr.92 and FC92–N (not observed in other cases), expressed as a high population of small cavities having radius of ~2 nm, indicates an extension in the duration of transient regimes. This further strengthens the explanation that higher levels of ~280 appm He can be attributed to the inhibited cavity growth; as a result, suppressed swelling even an increment in dose of 140 dpa. This interpretation aligns well with the expected effect of high-concentration helium from literature [15,23,27,30], which encompasses the restriction of the growth of pre-existing cavities and the promotion of nucleation in newly-formed cavities, thereby impeding swelling behavior. Therefore, consideration should be given to the inhibition of cavity growth induced by an excess amount of pre-implanted helium when designing similar ion-irradiation experiments. Although a clear onset point, where the implanted helium atoms begin to suppress swelling by hindering cavity growth, remains indeterminate, employing the dpa-following helium concentration approach may lead to unexpected helium-induced growth inhibition within the range of 100–200 appm He, as demonstrated in this study and corroborated by existing literature.

5. Conclusion

The radiation response of FC92 steels was comparatively studied alongside HT9 and Gr.92 utilizing heavy ion accelerator. The irradiation was performed up to 120 and 240 dpa, employing 3.5 MeV Fe^{++} ion at 475 °C, with a helium pre-implantation of 1 appm/dpa. Post-irradiation microstructure characterization was carried out, with a particular focus on cavity evolution, utilizing FE-TEM. The results of the present swelling were compared with our previous work on swelling behaviors in HT9, Gr.92, and FC92 series irradiated to 480 dpa at 475 °C, with a pre-implanted helium content of 1 appm/dpa.

(1) FC92 steel exhibited excellent swelling resistance after irradiation to 240 dpa, showing less swelling compared to HT9 and Gr.92. The volumetric swelling in the irradiated alloys reached 1.3 % in FC92–B and 0.8 % in FC92–N at 70 dpa, while it reached 7.4 % in HT9, 6.3 % in Gr.92, 2.9 % in FC92–B, and 3.6 % in FC92–N at 140 dpa, respectively. This lower swelling in FC92 series can be attributed to the suppression of both cavity nucleation and growth.

(2) After comparing the swelling behaviors at 140 dpa/140 appm He with swelling data at 280 dpa/280 appm He, it was observed that Gr.92 and FC92–N exhibited greater swelling at the 140 dpa/140 appm He condition than at the 280 dpa/280 appm He condition, despite the dose increment of 140 dpa. These two alloys exhibited the higher population ratio of small-sized cavities around the critical radius at 280 dpa/280 appm He, resulting in the bimodal cavity size distribution. In contrast, other dose/alloy combinations followed the Gaussian-like unimodal size distribution with only a sparse population of small-sized cavities. This negative correlation between dose and swelling can be attributed to the suppressed swelling at 280 dpa/280 appm He, as a result of helium-associated enhancement of cavity nucleation and inhibition of cavity growth.

Funding

This research was supported by the National Research Foundation of Korea (NRF) grant funded by the Ministry of Science, ICT, and Future Planning (MSIP) [grant number NRF-2016M2BA9912471] and Basic Science Research Program through the NRF funded by MSIP [grant number NRF-2016R1A5A1013919].

CRediT authorship contribution statement

Myeongkyu Lee: Conceptualization, Data curation, Formal analysis,

Funding acquisition, Investigation, Methodology, Resources, Software, Validation, Visualization, Writing – original draft, Writing – review & editing. **Geon Kim:** Data curation, Methodology, Software. **Sangjoon Ahn:** Conceptualization, Funding acquisition, Project administration, Supervision.

Declaration of competing interest

The authors declare that they have no known competing financial interests or personal relationships that could have appeared to influence the work reported in this paper.

Acknowledgments

The authors appreciate the KAERI for providing the tested F/M steel specimens and gratefully acknowledge Drs. L. Shao, J. Gigax, and H. Kim for their help with irradiations at Texas A&M university.

Appendix A. Supplementary data

Supplementary data to this article can be found online at https://doi.org/10.1016/j.net.2024.05.014.

References

[1] K.L. Murty, I. Charit, Structural materials for Gen-IV nuclear reactors: challenges and opportunities, J. Nucl. Mater. 383 (2008) 189–195.
[2] S.J. Zinkle, L.L. Snead, Opportunities and limitations for ion beams in radiation effects studies: bridging critical gaps between charged particle and neutron irradiations, Scr Mater 143 (2018) 154–160, https://doi.org/10.1016/j.scriptamat.2017.06.041.
[3] G.S. Was, Challenges to the use of ion irradiation for emulating reactor irradiation, J. Mater. Res. 30 (2015) 1158.
[4] F.A. Garner, L. Shao, M.B. Toloczko, S.A. Maloy, V.N. Voyevodin, Use of self-ion bombardment to study void swelling in advanced radiation-resistant alloys, in: 17th Int. Symp. Conf. On Environmental Degradation of Materials in Nuclear Power Systems, Ottawa, Canada, 2015.
[5] R.L. Klueh, D.R. Harries, High-chromium Ferritic and Martensitic Steels for Nuclear Applications, AsTM, West Conshohocken, PA, 2001.
[6] F. Masuyama, History of power plants and progress in heat resistant steels, ISIJ Int. 41 (2001) 612–625.
[7] W.J. Carmack, D.L. Porter, Y.I. Chang, S.L. Hayes, M.K. Meyer, D.E. Burkes, C. B. Lee, T. Mizuno, F. Delage, J. Somers, Metallic fuels for advanced reactors, J. Nucl. Mater. 392 (2009) 139–150, https://doi.org/10.1016/j.jnucmat.2009.03.007.
[8] S.H. Kim, J.H. Kim, S.G. Park, S.H. Shin, W.S. Ryu, Fabrication and Evaluation of Advanced Cladding Tube for PGSFR, (n.d.).
[9] O. Anderoglu, T.S. Byun, M. Toloczko, S.A. Maloy, Mechanical performance of ferritic martensitic steels for high dose applications in advanced nuclear reactors, Metall. Mater. Trans. 44 (2013) 70–83.
[10] J.F. Ziegler, M.D. Ziegler, J.P. Biersack, SRIM–The stopping and range of ions in matter (2010), Nucl. Instrum. Methods Phys. Res. B 268 (2010) 1818–1823.
[11] N.R.T. Astm, Standard practice for neutron radiation damage simulation by charged-particle irradiation, Annu. Book ASTM Stand. 12 (1996) E521.
[12] R.E. Stoller, M.B. Toloczko, G.S. Was, A.G. Certain, S. Dwaraknath, F.A. Garner, On the use of SRIM for computing radiation damage exposure, Nucl. Instrum. Methods Phys. Res. B 310 (2013) 75–80.
[13] T. Malis, S.C. Cheng, R.F. Egerton, EELS log-ratio technique for specimen-thickness measurement in the TEM, J. Electron. Microsc. Tech. 8 (1988) 193–200, https://doi.org/10.1002/jemt.1060080206.
[14] L. Shao, C.-C. Wei, J. Gigax, A. Aitkaliyeva, D. Chen, B.H. Sencer, F.A. Garner, Effect of defect imbalance on void swelling distributions produced in pure iron irradiated with 3.5 MeV self-ions, J. Nucl. Mater. 453 (2014) 176–181.
[15] E. Getto, Z. Jiao, A.M. Monterrosa, K. Sun, G.S. Was, Effect of pre-implanted helium on void swelling evolution in self-ion irradiated HT9, J. Nucl. Mater. 462 (2015) 458–469.
[16] A.D. Brailsford, L.K. Mansur, Effect of self-ion injection in simulation studies of void swelling, J. Nucl. Mater. 71 (1977) 110–116.
[17] D.L. Plumton, W.G. Wolfer, Suppression of void nucleation by injected interstitials during heavy ion bombardment, J. Nucl. Mater. 120 (1984) 245–253.
[18] M. Lee, G. Kim, Y. Jung, S. Ahn, Radiation-induced swelling and precipitation in Fe ++ ion-irradiated ferritic/martensitic steels, J. Nucl. Mater. (2021) 153137.
[19] M.P. Short, D.R. Gaston, M. Jin, L. Shao, F.A. Garner, Modeling injected interstitial effects on void swelling in self-ion irradiation experiments, J. Nucl. Mater. 471 (2016) 200–207.
[20] F. Abe, T.-U. Kern, R. Viswanathan. Creep-resistant Steels, Elsevier, 2008.
[21] F. Abe, Precipitate design for creep strengthening of 9% Cr tempered martensitic steel for ultra-supercritical power plants, Sci. Technol. Adv. Mater. 9 (2008) 13002.
[22] A. Bhattacharya, S.J. Zinkle, J. Henry, S.M. Levine, P.D. Edmondson, M.R. Gilbert, H. Tanigawa, C.E. Kessel, Irradiation damage concurrent challenges with RAFM and ODS steels for fusion reactor first-wall/blanket: a review, J. Phys. Energy 4 (2022) 034003.
[23] A.M. Monterrosa, Z. Jiao, G.S. Was, The influence of helium on cavity evolution in ion-irradiated T91, J. Nucl. Mater. 509 (2018) 707–721.
[24] A. Hishinuma, L.K. Mansur, Critical radius for bias-driven swelling—a further analysis and its application to bimodal cavity size distributions, J. Nucl. Mater. 118 (1983) 91–99.
[25] L.L. Horton, L.K. Mansur, Experimental Determination of the Critical Cavity Radius in Fe-10Cr for Ion Irradiation, ASTM International, 1985.
[26] Y.-R. Lin, A. Bhattacharya, D. Chen, Y. Zhao, J.-J. Kai, J. Henry, S.J. Zinkle, The role of Cr concentration and temperature on cavity swelling with co-injected helium in dual-ion irradiated Fe and Fe-Cr alloys, Mater. Des. 223 (2022) 111134.
[27] Y.-R. Lin, A. Bhattacharya, S.J. Zinkle, The effect of helium on cavity swelling in dual-ion irradiated Fe and Fe-10Cr ferritic alloys, J. Nucl. Mater. 569 (2022) 153907.
[28] A. Bhattacharya, S.J. Zinkle, Cavity swelling in irradiated materials, in: Reference Module in Materials Science and Materials Engineering, 2020, https://doi.org/10.1016/B978-0-12-803581-8.11599-1.
[29] G.S. Was, Fundamentals of Radiation Materials Science: Metals and Alloys, springer, 2016.
[30] K. Farrell, M.B. Lewis, N.H. Packan, Simultaneous bombardment with helium, hydrogen, and heavy ions to simulate microstructural damage from fission or fusion neutrons, Scripta Metall. 12 (1978) 1121–1124, https://doi.org/10.1016/0036-9748(78)90087-X.
[31] M.J. Caturla, C.J. Ortiz, C.C. Fu, Helium and point defect accumulation:(ii) kinetic modelling, C R Phys 9 (2008) 401–408.
[32] C.-C. Fu, F. Willaime, Ab initio study of helium in α− Fe: dissolution, migration, and clustering with vacancies, Phys. Rev. B 72 (2005) 064117.